

Chapter 13

Density Calculation of Pseudo Breast MRI Based on Adversarial Generative Network



Yuanzhen Liu, Wei Lin, and Yujia Cheng

Abstract In this paper is proposed a method for mammographic percentage density (PD%) calculation from reconstructed pseudo MRI from real breast MRI. Firstly, the mammography and real breast MRI data were collected from the same women in one year. Then, a direct mapping model was constructed from mammographic to another breast MRI by Gan, and we called the generated MRI pseudo breast MRI. Secondly, a U-Net was used to segment the ROI on the pseudo breast MRI, so that the PD% can be obtained. Finally, DSC was used to evaluate the mapping model and the U-Net, and linear regression and Pearson correlation coefficient were used to evaluate the PD%. The results showed that the average DSC in the breast region and fibro-glandular tissues were 0.937 and 0.853, respectively. In addition, the PD% of the pseudo breast MRI was 2.576%, and the average accuracy between real and pseudo breast MRI images was 0.987.

13.1 Introduction

Mammography is the first major means of breast cancer screening and plays an important role in reducing the mortality of female breast cancer. As early as 1976, Wolfe [1, 2] proposed that Mammographic breast density (MBD) can be used as an independent risk factor for breast cancer. Later, studies by scholars Park and Eriksson [3, 4] showed that gland density was a major risk factor for new and recurrent breast cancer. Gland density is described and recorded as an important sign in ACRBI-RADS (Breast imaging reporting and data system) classification. It is obvious that it is very important to accurately evaluate the density of female breast glands.

In the 2017 China Cancer report, China revealed that the incidence of female breast cancer is also the first among malignant tumors, and the risk of breast cancer among women in big cities is nearly twice as high as that in small cities [5], and the mortality rate is much higher than that in the United States. Although the relationship

Y. Liu · W. Lin (✉) · Y. Cheng
Shanghai Institute of Technology, Shanghai 0086, China
e-mail: linwei_0622@aliyun.com

between gland density and the molecular and biological mechanism of breast cancer is still being studied, breast gland density is an important factor affecting breast cancer screening sensitivity and prevention risk prediction. Literature [6] reported that the sensitivity of breast X-ray to detect lesions in fatty and dense glands decreased from 87 to 62.9%. Women with dense glands have a 4.64 times higher risk of breast cancer during their lifetime than women with low gland density due to the increased density of glands and due to their rich glandular matrix [7].

The clinical evaluation of the density of female glands has always been observed by doctors with the naked eye, and the four grades of ABCD of glands have been quantitatively evaluated according to the BI-RADS standard based on experience. In the past, it was difficult to evaluate accurately and quantitatively on the two-dimensional image of mammography. Lehman and Fieselmann [8, 9] have shown that the quantitative evaluation of gland content by computer on breast X-ray images is highly consistent with that by doctors' naked eyes, which indicates that it is reliable to use a computer to quantify glands in a clinic. Quantitative calculation of glands is more accurate. Studies by Ng and Lau et al. [10] confirmed that no matter what equipment was used to examine the glands of the same woman in one year, the physical quantity of the glands was the same. Bonmat et al. [11] used the same female breast X-ray and breast MRI examination to register 2D and 3D gland images obtained by the two examination modes, so as to obtain accurate quantification of glands on conventional breast X-ray images, which makes it possible to quantitatively evaluate glands on breast X-ray images. The advantage of measuring breast density by breast X-ray image lies in its low cost and wide use. Lu [12] comparing breast MRI with breast X-ray images stated that the quantitative evaluation of glands in the same woman has a high consistency within a certain period of time. In order to obtain accurate gland content, segmentation is very important. This study attempts to find the mapping relationship between mammography and breast MRI and to establish a mapping model between mammography and breast MRI. At present, there is little similar work in the literature; firstly, the breast x-ray image is mapped to the pseudo breast MRI image through the mapping model.

13.2 Material and Methods

The proposed method for calculating mammographic PD% consists of the following core steps:

- a. Preprocessing of mammographic images about the breast;
- b. Reconstruction of mammographic image based on real breast MRI.
- c. ROI segmentation and PD% calculation.

MRI data were taken from more than 500 patients at different times in a year, with an average of more than two times per patient. The mammography data used in this experiment were synthesized by breast MRI images mentioned above. Real breast MRI data in this study were all obtained from open source. Breast MRI was

performed on 1.5-T scanner (signa, GE Healthcare, Milwaukee, WI) with a bilateral phased array breast coil. Approximately 120 + cases were sorted out from the data collected, each of which contained 60 slices.

13.2.1 Preprocessing of Images About the Breast

During preprocessing of medical images, low-quality images were manually eliminated, so that the adverse impact brought by the original image on the mapping model could be evaded. The breast MRI images were denoised by CBDNet, designed by Kai Zhang's team for real photograph denoising in 2019 [13–15]. It is mainly composed of two parts, one is the noise generation network, which generates an estimated noise image from the input; and the other is a U-Net denoising network (Fig. 13.1). In CBDNet, the original image and noise image predicted by the noise generation network were sent into the second network for denoising.

In order to achieve CBDnet denoising, it was necessary to denoise the original breast MRI manually to create a dataset. In our study, a professional software to view and process medical images (Radiant DICOM Viewer) was used to denoise the original breast MRI images. The prepared dataset was then substituted into CBDNet inputting, and the denoising outcome was shown in Fig. 13.2.

There were 60 slices in the breast MRI dataset, containing information about the entire breast. The mapping model between mammography and breast MRI was implemented by Generative Adversarial Networks (GAN). Only 12 breast MRI slices

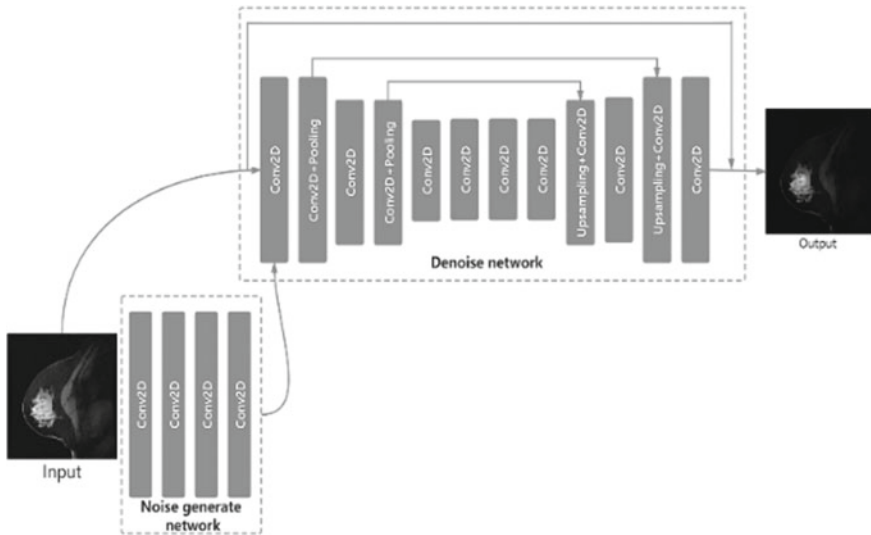


Fig. 13.1 The structure of a CBDNet

Fig. 13.2 Denoising outcome of CBDNet: **a** original breast MRI image and **b** the same MRI images denoised by CBDNet

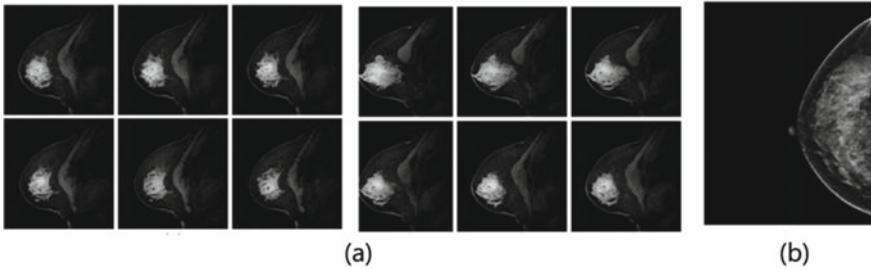
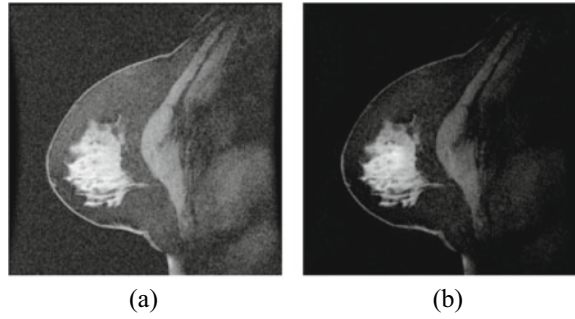


Fig. 13.3 An example of mammography image constructed with breast MRI: **a** 12 slices of breast MRI and **b** the constructed mammography image

were selected for one MRI sample, and they must be physically continuous and as close to the breast center as possible, which was set to exhibit a linear decrease along with its slice number, so as to imitate the attenuation of X-ray energy inside human body during medical X-ray imaging. Breast MRI slices and a sample mammography image are shown in Fig. 13.3.

13.2.2 Construction of the Mapping Model from Mammography to MRI

In this study, we try to generate several breast MRI slices from one mammography image by a mapping model, and GAN was a good tool to realize that [16]. In our model, we planned to set mammography images as inputs, and the output (target) was designed to be 12 breast MRI slices. For GAN, pix-to-pix was a typical one-to-one correlation in previous researches [17], which successfully tackles the problem of realized one-to-one image transformations.

Parameters to generate our GAN went as follows: input dimension was one (for mammography), the output dimension was 12 (for 12 breast MRI slices). When generating DCGan [18], the input was a small dimension of the noise data, and the

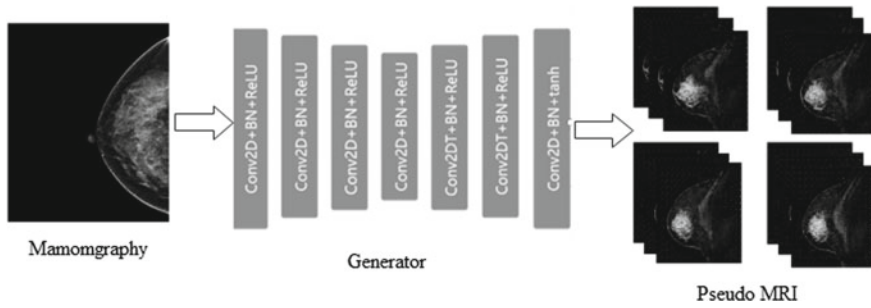


Fig. 13.4 Generator network

target image was output by sampling and increasing dimensions on the convolution layer. Procedures of dimensional reduction and increase correspond to encoding and decoding in the encoder [19], and the generator network is demonstrated in Fig. 13.4.

For the discriminator network, its parameters went as follows: input dimension was 24 (12 real or pseudo breast MRI plus 12 real MRI images), and the output dimension was one, which represented the probability of all the current input. The structure of our discriminator network is shown in Fig. 13.5.

Based on the GAN structures, binary cross-entropy loss function was selected to describe the generator and discriminator networks. The prepared mammography and breast MRI images were put into the GAN network for training, and Fig. 13.6 illustrates the outcome after 20,000 times of alternating training between the two networks.

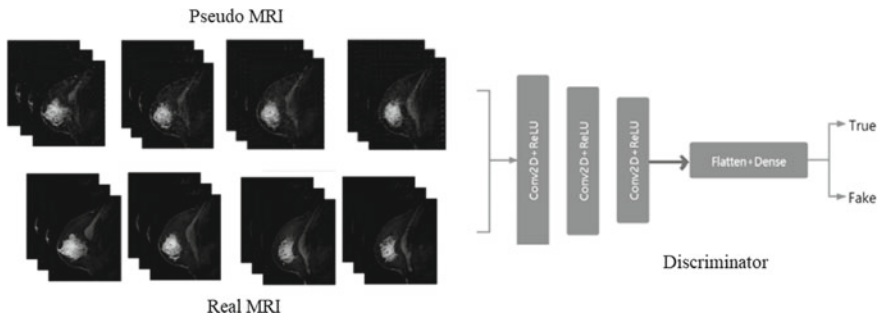


Fig. 13.5 Discriminator network

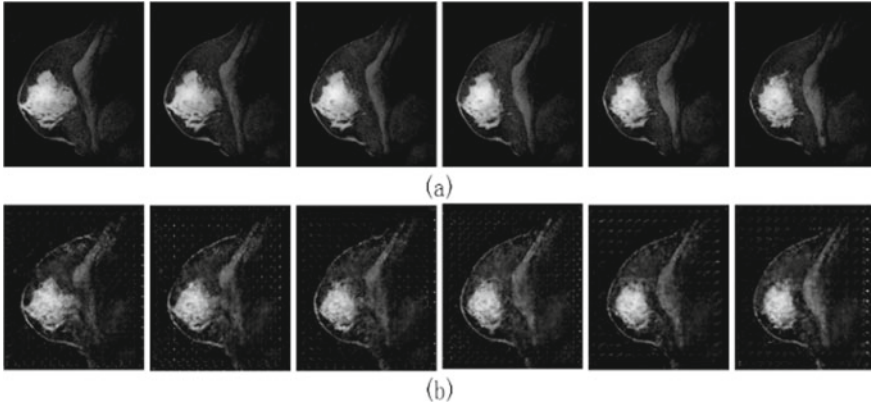


Fig. 13.6 Outcome of applying mapping model on breast MRI: **a** real breast MRI and **b** pseudo breast MRI generated by mapping model

13.2.3 ROI Segmentation and PD% Calculation

In this study, U-Net was used to segment breast regions and fibro-glandular tissue from breast MRI for further PD% calculations. Mask data was needed for training U-Net to automatically achieve such operations, and we used a software called Labelme to create mask datasets (Fig. 13.7). The K-means algorithm was used to realize binarization for the fibro-glandular region, which were implemented as follows [20]:

- a. K cluster centers were randomly initialized.
- b. While the centers of K clusters moved:
 - I. Calculate their distances to reach all samples.
 - II. Separate the samples by their nearest clusters.
 - III. Recalculate cluster centers.

Repeat this process until centers didn't move anymore.

- c. And the results were output.

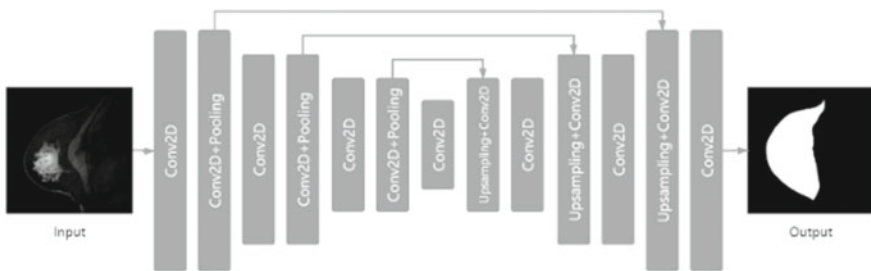


Fig. 13.7 Structure of the U-Net

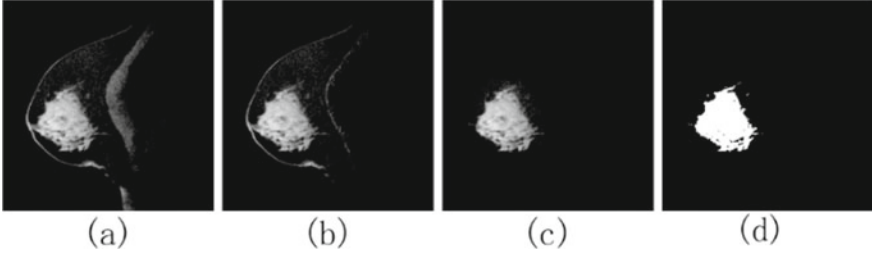


Fig. 13.8 Outcome of U-net segmentation: **a** original breast MRI, **b** breast region, **c** fibro-glandular tissue region, and **d** binarization result from

The region reflecting the fibro-glandular tissue was separated from the background with K-means algorithm, and $K = 2$. The segmentation outcome is shown in Fig. 13.8.

FGT% is defined as the relative volume percentage of fibro-glandular tissue within the breast, and it is calculated as:

$$PD\% = FGT\% = \frac{|FGT|}{|Breast|} \times 100 \quad (13.1)$$

13.2.4 Validation

The effect of U-Net segmentation on breast and fibro-glandular tissue was evaluated by the DSC difference between regions obtained by manual definitions and U-Net, which was a common parameter for this application. It will directly affect the PD% and the evaluation results of our mapping model, taking U-Net segmentation results on breast region as an example.

$$s = \frac{2|A \cap B|}{|A| + |B|} \quad (13.2)$$

where A was the manually defined breast region and B was the breast region after U-Net segmentation. The closer the DSC is to 1, the better effect U-Net segmentation produces.

PD% values were calculated for both pseudo and real breast MRI images to evaluate the pseudo's effectiveness. Linear regression and Pearson's correlation coefficients were used to evaluate the correlation of PD%, and the calculation was carried out by the following equation:

$$r = \frac{N \sum x_i y_i - \sum x_i \sum y_i}{\sqrt{N \sum x_i^2 - (\sum x_i)^2} \sqrt{N \sum y_i^2 - (\sum y_i)^2}} \quad (13.3)$$

where x is the PD content of real breast and Y is the gland content calculated by the algorithm.

In order to evaluate the stability of our method of calculation, identical procedures were carried out on the same patient at different times in a year. The smaller the numerical changes of breast PD% obtained were, the more stable the calculation method was.

13.3 Experiments and Results

13.3.1 *Evaluation of the Mapping Model from Mammography to Breast MRI Images*

DSC was used to evaluate the spatial consistency between real and pseudo breast MRI images as a reflection of the mapping model's performance. In one experiment, breast and fibro-glandular tissue regions were segmented from 30 random real images of their corresponding pseudo ones, followed by subsequent calculations for mean DSC. A total of ten experiments were conducted, and the results are shown in Table 13.1. The overall mean DSC was 0.937 with a mean standard deviation of 0.0069 (mean standard deviation) for the breast region in real and pseudo MRI images. For real and pseudo fibro-glandular tissue regions, the overall mean DSC was 0.8509, and the mean standard deviation of 0.039. Therefore, we could conclude that our mapping model is significantly less effective for the fibro-glandular tissue.

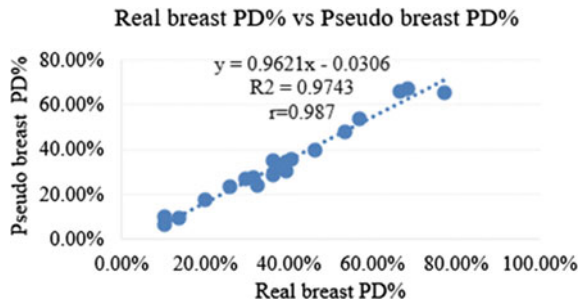
Table 13.1 DSC calculations of breast and fibro-glandular tissue in real and pseudo MRI images

No	Breast region				Breast fibro-glandular tissue			
	Average	Max	Min	Standard Deviation	Average	Max	Min	Standard Deviation
1	0.938	0.956	0.929	0.008	0.836	0.904	0.761	0.049
2	0.938	0.950	0.928	0.007	0.839	0.883	0.773	0.032
3	0.936	0.956	0.921	0.010	0.871	0.924	0.797	0.035
4	0.937	0.948	0.928	0.006	0.851	0.911	0.755	0.047
5	0.936	0.954	0.919	0.012	0.839	0.885	0.773	0.037
6	0.941	0.956	0.931	0.006	0.844	0.884	0.791	0.030
7	0.935	0.950	0.924	0.009	0.857	0.911	0.777	0.044
8	0.938	0.953	0.925	0.008	0.857	0.899	0.796	0.035
9	0.938	0.955	0.924	0.008	0.870	0.924	0.815	0.036
10	0.936	0.953	0.924	0.008	0.845	0.911	0.764	

Table 13.2 PD% calculations of breast and fibro-glandular tissue in real and pseudo MRI

No	Real PD%	Pseudo PD%	Error (%)	Max error (%)	Min error (%)	Average error (%)
1	57.01	53.64	3.37	5.97	0.28	2.576
2	66.49	66.21	0.28			
3	20.10	17.37	2.73			
4	36.36	35.39	0.97			
5	31.65	27.72	3.93			
6	10.45	9.87	0.58			
7	25.80	23.41	2.39			
8	68.38	67.17	1.21			
9	13.70	9.37	4.33			
10	36.91	31.12	5.97			

Fig. 13.9 Linear regression results for PD% between real and pseudo MRI



13.3.2 Evaluation of the Breast PD%

Table 13.2 showed the breast PD% of ten data in the test dataset, and the maximum, minimum, and average errors of PD% were 5.97%, 0.28%, and 2.576% between real and pseudo MRI images, respectively. In order to further explore the stability for PD% calculation, 20 patients were randomly selected from the data set, and their breast PD% values were calculated based on the method mentioned with linear regression and the results are shown in Fig. 13.9.

13.4 Discussion

In this study, a GAN-based mapping model between mammography and breast MRI was constructed, providing a new way to calculate PD%. It can directly transform mammography images into pseudo breast MRI, and then segment the breast and fibro-landular tissue regions, enabling easy calculations for the breast PD%.

Calculation results for DSC verify the effectiveness of our model. In terms of breast PD% calculation, the breast density and error analysis show that real and pseudo breast MRI images are highly consistent and correlated, suggesting actual feasibility for 3D reconstruction results from mammography to be applied as MRI images in actual practice.

Further efforts could focus on building a more promising mapping model to generate pseudo breast MRI images with higher quality, so that a more accurate fibro-glandular tissue segmentation could be achieved.

References

1. Wolfe, J.N., Chief, M.D.: Risk for breast cancer development determined by mammographic parenchymal pattern. *Cancer* **37**(5), 2486–2492 (1976)
2. Wolfe, J.N.: Breast patterns as an index of risk for developing breast cancer. *Am. J. Roentgenol* **126**, 1130–1137 (1976)
3. Eriksson, L., Czene, K., Rosenberg, L.U., Törnberg, S., Humphreys, K., Hall, P.: Mammographic density and survival in interval breast cancers. *Breast Cancer Res.* **15**(3), 48 (2013)
4. Park, C.C., Rembert, J., Chew, K., Moore, D., Kerlikowske, K.: High mammographic breast density is independent predictor of local for invasive breast cancer. *Int. J. Radiat. Oncol. Biol. Phys.* **73**(1), 5–79 (2009)
5. Chen, W.Q., Zheng, R.S., Zhang, S.W.: Cancer incidence and mortality in China in 2013: an analysis based on urbanization level. *Chin. J. Cancer Res.* **29**(1), 1–10 (2017)
6. Carney, P.A., Miglioretti, D.L., Yankaskas, B.C., Kerlikowske, K.: Individual and combined effects of age, breast density, and hormone replacement therapy use on the accuracy of screening mammography. *Ann. Intern. Med.* **138**(3), 168–175 (2003)
7. McCormack, V.A., dos Santos Silva, I.: Breast density and parenchymal patterns as markers of breast cancer risk: a meta-analysis. *Cancer Epidemiol. Biomarkers* **15**(6), 1159–1169 (2006)
8. Lehman, C.D., Yala, A., Schuster, T., Dontchos, B., Barzilay, R.: Mammographic breast density assessment using deep learning: clinical implementation. *Radiology* **290**(1), 52–58 (2018)
9. Fieselmann, A., Frnvik, D., Lng, K.: Volumetric breast density measurement for personalized screening: accuracy, reproducibility, consistency, and agreement with visual assessment. *J. Med. Imaging* **6**(3), 031406 (2019)
10. Ng, K.H., Lau, S.: Vision 20/20: Mammographic breast density and its clinical applications. *Med. Phys.* **43**(12), 7059–7077 (2015)
11. Marcos, E.G.: Glandular tissue pattern analysis through multimodal MRI-mammography registration. M.S. thesis, Univ (2018)
12. Lu, L.J.W., Nishino, T.K.: Comparison of breast tissue measurements using magnetic resonance imaging, digital mammography and a mathematical algorithm. *Phys. Med. Biol.* **57**(21), 6903–6927 (2012)
13. Zhang, K., Zuo, W.M., Chen, Y.J., Meng, D., Zhang, L.: Beyond a Gaussian denoiser: residual learning of deep CNN for image denoising. *IEEE Trans. Image Process* **26**(7), 3142–3155 (2017)
14. Zhang, K., Zuo, W.M., Zhang, L.: FFDNet: toward a fast and flexible solution for CNN-based image denoising. *IEEE Trans. Image Process.* **27**(4), 4608–4622 (2018)
15. Guo, S., Yan, Z., Zhang, K., Zuo, W.M., Zhang, L.: Toward convolutional blind denoising of real photographs. In: *CVPR 2019*, pp. 1712–1722 (2019)
16. Goodfellow, I.J., Abadie, J.P., Mirza, M., Xu, B.: Generative adversarial nets. In: *NIPS 2014*, Montreal, QC, Canada, pp. 2672–2680 (2014)

17. Isola, P., Zhu, J.Y., Zhou, T., Efros, A.: Image-to-image translation with conditional adversarial networks. In: CVPR 2017, Honolulu, HI, pp. 1125–1134 (2017)
18. Radford, A., Metz, L., Chintala, S.: Unsupervised representation learning with deep convolutional generative adversarial networks. arXiv preprint arXiv 1511.06434 (2015)
19. Vincent, P., Larochelle, H., Bengio, Y., Manzagol, P.A.: Extracting and composing robust features with denoising autoencoders. In: 25th ICML 2008, Helsinki, pp. 1096–1103, Finland (2008)
20. Kanungo, T., Mount, D.M., Netanyahu, N.S., Christine, C.D., Siverman, R., Angela, Y.: An efficient k-means clustering algorithm: analysis and implementation. *IEEE T. Pattern. Anal* **24**(7), 881–892 (2002)